Flexible flux plane simulations of parasitic absorption in nanoplasmonic thin-film silicon solar cells

H. Chung,[1] **K-Y. Jung,**[2] **and P. Bermel**[1,*]

[1]*Birck Nanotechnology Center, Electrical and Computer Engineering, 1205 W. State St, West Lafayette, Indiana*
[2] *Department of Electronic Engineering, Hanyang University, Seoul, South Korea*
∗pbermel@purdue.edu

Abstract: Photovoltaic light trapping theory and experiment do not always clearly demonstrate how much useful optical absorption is enhanced, as opposed to parasitic absorption that cannot improve efficiencies. In this work, we develop a flexible flux plane method for capturing these parasitic losses within finite-difference time-domain simulations, which was applied to three classical types of light trapping cells (e.g., periodic, random and plasmonic). Then, a 2 μm-thick c-Si cell with a correlated random front texturing and a plasmonic back reflector is optimized. In the best case, 36.60 mA/cm^2 J_{sc} is achieved after subtracting 3.74 mA/cm^2 of parasitic loss in a 2-μm-thick c-Si cell slightly above the Lambertian limit.

OCIS codes: (350.4238) Nanophotonics and photonic crystals; (350.6050) Solar energy.

References and links

1. P. Bermel, C. Luo, L. Zeng, L. C. Kimerling, and J. D. Joannopoulos, "Improving thin-film crystalline silicon solar cell efficiencies with photonic crystals," Opt. Express **15**, 16986–17000 (2007).
2. M. A. Green, "Lambertian light trapping in textured solar cells and light-emitting diodes: analytical solutions," Prog. Photovolt.: Res. Appl. **10**, 235–241 (2002).
3. V. E. Ferry, M. A. Verschuuren, H. B. Li, E. Verhagen, R. J. Walters, R. E. Schropp, H. A. Atwater, and A. Polman, "Light trapping in ultrathin plasmonic solar cells," Opt. Express **18**, A237–A245 (2010).
4. X. Wang, M. R. Khan, J. L. Gray, M. A. Alam, and M. S. Lundstrom, "Design of GaAs solar cells operating close to the shockley-queisser limit," IEEE J. Photovolt. **3**, 737–744 (2013).
5. X. Wang, M. R. Khan, M. A. Alam, and M. Lundstrom, "Approaching the shockley-queisser limit in gaas solar cells," in "38th Photovoltaic Specialists Conference (PVSC)," (IEEE, 2012), pp. 002117–002121.
6. H. Sai, H. Jia, and M. Kondo, "Impact of front and rear texture of thin-film microcrystalline silicon solar cells on their light trapping properties," J. Appl. Phys. **108**, 044505 (2010).
7. H. Sai, H. Fujiwara, M. Kondo, and Y. Kanamori, "Enhancement of light trapping in thin-film hydrogenated microcrystalline si solar cells using back reflectors with self-ordered dimple pattern," Appl. Phys. Lett. **93**, 143501 (2008).
8. H. Sai and M. Kondo, "Effect of self-orderly textured back reflectors on light trapping in thin-film microcrystalline silicon solar cells," J. Appl. Phys. **105**, 094511 (2009).
9. G. Yue, L. Sivec, J. M. Owens, B. Yan, J. Yang, and S. Guha, "Optimization of back reflector for high efficiency hydrogenated nanocrystalline silicon solar cells," Appl. Phys. Lett. **95**, 263501 (2009).
10. H. Tan, R. Santbergen, A. H. Smets, and M. Zeman, "Plasmonic light trapping in thin-film silicon solar cells with improved self-assembled silver nanoparticles," Nano Lett. **12**, 4070–4076 (2012).
11. H. Tan, L. Sivec, B. Yan, R. Santbergen, M. Zeman, and A. H. Smets, "Improved light trapping in microcrystalline silicon solar cells by plasmonic back reflector with broad angular scattering and low parasitic absorption," Appl. Phys. Lett. **102**, 153902 (2013).
12. E. Yablonovitch, "Statistical ray optics," J. Opt. Soc. Am. **72**, 899–907 (1982).

13. S. E. Han and G. Chen, "Toward the lambertian limit of light trapping in thin nanostructured silicon solar cells," Nano Lett. **10**, 4692–4696 (2010).
14. V. E. Ferry, A. Polman, and H. A. Atwater, "Modeling light trapping in nanostructured solar cells," ACS Nano **5**, 10055–10064 (2011).
15. Y. Zhang, Z. Ouyang, N. Stokes, B. Jia, Z. Shi, and M. Gu, "Low cost and high performance Al nanoparticles for broadband light trapping in si wafer solar cells," Appl. Phys. Lett. **100**, 151101 (2012).
16. A. Tamang, A. Hongsingthong, P. Sichanugrist, V. Jovanov, M. Konagai, and D. Knipp, "Light-trapping and inter-face morphologies of amorphous silicon solar cells on multiscale surface textured substrates," IEEE J. Photovolt. **4**, 16–21 (2013).
17. M. G. Deceglie, V. E. Ferry, A. P. Alivisatos, and H. A. Atwater, "Design of nanostructured solar cells using coupled optical and electrical modeling," Nano Lett. **12**, 2894–2900 (2012).
18. A. Naqavi, K. Söderström, F.-J. Haug, V. Paeder, T. Scharf, H. P. Herzig, and C. Ballif, "Understanding of photocurrent enhancement in real thin film solar cells: towards optimal one-dimensional gratings," Opt. Express **19**, 128–140 (2011).
19. O. Isabella, S. Solntsev, D. Caratelli, and M. Zeman, "3-D optical modeling of thin-film silicon solar cells on diffraction gratings," Prog. Photovolt.: Res. Appl. **21**, 94–108 (2013).
20. R. Dewan, V. Jovanov, C. Haase, H. Stiebig, and D. Knipp, "Simple and fast method to optimize nanotextured interfaces of thin-film silicon solar cells," Appl. Phys. Express **3**, 092301 (2010).
21. K. Jäger, M. Fischer, R. A. van Swaaij, and M. Zeman, "Designing optimized nano textures for thin-film silicon solar cells," Opt. Express **21**, A656–A668 (2013).
22. V. E. Ferry, M. A. Verschuuren, H. B. Li, R. E. Schropp, H. A. Atwater, and A. Polman, "Improved red-response in thin film a-si: H solar cells with soft-imprinted plasmonic back reflectors," Appl. Phys. Lett. **95**, 183503 (2009).
23. A. F. Oskooi, D. Roundy, M. Ibanescu, P. Bermel, J. D. Joannopoulos, and S. G. Johnson, "Meep: A flexible free-software package for electromagnetic simulations by the fdtd method," Comp. Phys. Comm. **181**, 687–702 (2010).
24. R. S. Sesuraj, T. Temple, and D. Bagnall, "Optical characterisation of a spectrally tunable plasmonic reflector for application in thin-film silicon solar cells," Solar Energy Mat. and Solar Cells **111**, 23–30 (2013).
25. H. Chung, K. Jung, X. Tee, and P. Bermel, "Time domain simulation of tandem silicon solar cells with optimal textured light trapping enabled by the quadratic complex rational function," Opt. Express **22**, A818–A832 (2014).
26. T. G. Jurgens and A. Taflove, "Three-dimensional contour FDTD modeling of scattering from single and multiple bodies," IEEE Trans. Antennas Propag. **41**, 1703–1708 (1993).
27. T. Jurgens, A. Taflove, K. Umashankar, and T. Moore, "Finite-Difference Time-Domain modeling of curved surfaces," IEEE Trans. Antennas Propag. **40**, 357–366 (1992).
28. N. Kaneda, B. Houshmand, and T. Itoh, "Fdtd analysis of dielectric resonators with curved surfaces," IEEE Trans. Microwave Theory Tech. **45**, 1645–1649 (1997).
29. E. Neufeld, N. Chavannes, T. Samaras, and N. Kuster, "Novel conformal technique to reduce staircasing artifacts at material boundaries for fdtd modeling of the bioheat equation," Phys. Medicine and Biology **52**, 4371 (2007).
30. E. Hallynck and P. Bienstman, "Photonic crystal biosensor based on angular spectrum analysis," Opt. Express **18**, 18164–18170 (2010).
31. J. Nadobny, D. Sullivan, P. Wust, M. Seebaß, P. Deuflhard, and R. Felix, "A high-resolution interpolation at arbitrary interfaces for the fdtd method," IEEE Trans. Microwave Theory Tech. **46**, 1759–1766 (1998).
32. M. T. Bettencourt, "Flux limiting embedded boundary technique for electromagnetic fdtd," J. Comp. Phys. **227**, 3141–3158 (2008).
33. H. Chung, S. Ha, J. Choi, and K. Jung, "Accurate FDTD modelling for dispersive media using rational function and particle swarm optimisation," Int. J. Electronics **102**, 1218–1228 (2015)
34. V. E. Ferry, M. A. Verschuuren, M. C. v. Lare, R. E. Schropp, H. A. Atwater, and A. Polman, "Optimized spatial correlations for broadband light trapping nanopatterns in high efficiency ultrathin film a-si: H solar cells," Nano Lett. **11**, 4239–4245 (2011).
35. F.-J. Haug, T. Söderström, M. Python, V. Terrazzoni-Daudrix, X. Niquille, and C. Ballif, "Development of micro-morph tandem solar cells on flexible low-cost plastic substrates," Solar Energy Mat. and Solar Cells **93**, 884–887 (2009).
36. H. Sai, K. Saito, N. Hozuki, and M. Kondo, "Relationship between the cell thickness and the optimum period of textured back reflectors in thin-film microcrystalline silicon solar cells," Appl. Phys. Lett. **102**, 053509 (2013).
37. L. Sivec, B. Yan, G. Yue, J. Owens-Mawson, J. Yang, and S. Guha, "Advances in light trapping for hydrogenated nanocrystalline silicon solar cells," IEEE J. Photovolt. **3**, 27–34 (2013).
38. R. Ren, Y. Guo, and R. Zhu, "Design of a plasmonic back reflector for silicon nanowire decorated solar cells," Opt. Lett. **37**, 4245–4247 (2012).
39. H. A. Atwater and A. Polman, "Plasmonics for improved photovoltaic devices," Nature Mat. **9**, 205–213 (2010).
40. P. Spinelli, V. Ferry, J. Van de Groep, M. Van Lare, M. Verschuuren, R. Schropp, H. Atwater, and A. Polman, "Plasmonic light trapping in thin-film si solar cells," J. Opt. **14**, 024002 (2012).
41. Z. Yu, A. Raman, and S. Fan, "Nanophotonic light-trapping theory for solar cells," Appl. Phys. A **105**, 329–339 (2011).

42. Z. Yu, A. Raman, and S. Fan, "Thermodynamic upper bound on broadband light coupling with photonic structures," Phys. Rev. Lett. **109**, 173901 (2012).
43. K. Knight, Mathematical Statistics (CRC Press, Boca Raton, Florida, 1999).

1. Introduction

There has been a strong trend in the solar industry toward thinner photovoltaic cells, particularly in the last decade. This has been driven not only by cost considerations, but also enabled by enhanced light trapping strategies [1–3] as well as the performance benefits associated with photon recycling [4, 5]. However, additional improvements in light trapping are needed for this approach to continue further, particularly in important solar materials with indirect bandgaps such as crystalline silicon (c-Si). The limits of current approaches such as random texturing [6] and plasmonic structures [3] should be considered, to see where particular opportunities for improvement may lie.

Figure 1 illustrates how three particular experimental light trapping schemes can enhance path length: periodic texturing on the front and back surfaces shown in Fig. 1(a) [7, 8], random texturing on the front and back surfaces shown in Fig. 1(b) [6, 9] and random texturing on the front surface combined with plasmonic nanoparticles (NPs) near the back surface shown in Fig. 1(c) [10, 11]. To date, incorporating these structures into 2 μm c-Si solar cells has resulted in experimentally measured short circuit currents between 22 and 29 mA/cm^2. [6–11]. However, it is believed that substantially better performance should be possible. The upper limit of light trapping for purely random texturing is known as the Lambertian limit, which represents a maximum enhancement of path length of $4n^2$ in weakly absorptive materials [12]; for 2 μm thick c-Si solar cells with perfect carrier collection, it would yield a short circuit current around 35 mA/cm^2 [13].

This gap between experiment and theory strongly implies that parasitic losses are occurring in these designs, which may be associated with metallic structures in the back [6, 9, 11]. Nevertheless, in most experiments, parasitic absorption was not considered [7] or was only indirectly measured by comparing the external quantum efficiency (EQE) with the absorption spectrum [6, 8–11]. However, EQE measurements cannot distinguish between optical and electronic losses (e.g., from recombination). On the other hand, simulation based approaches have
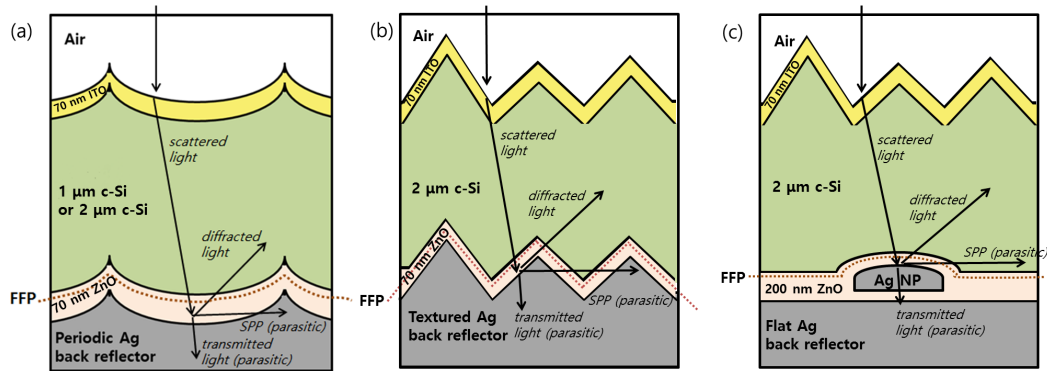

Fig. 1. Schematic illustration of three thin-film crystalline silicon light-trapping plasmonic structures: (a) periodic (grating-like) texturing on the front and back surfaces, deposited conformally; (b) random texturing on the front and back surfaces, deposited conformally; (c) random texturing on the front surface combined with plasmonic nanoparticles near the back surface. For the greatest speed, parasitic absorption is calculated using flexible flux planes instead of volumetric integration. (see Fig. 3)
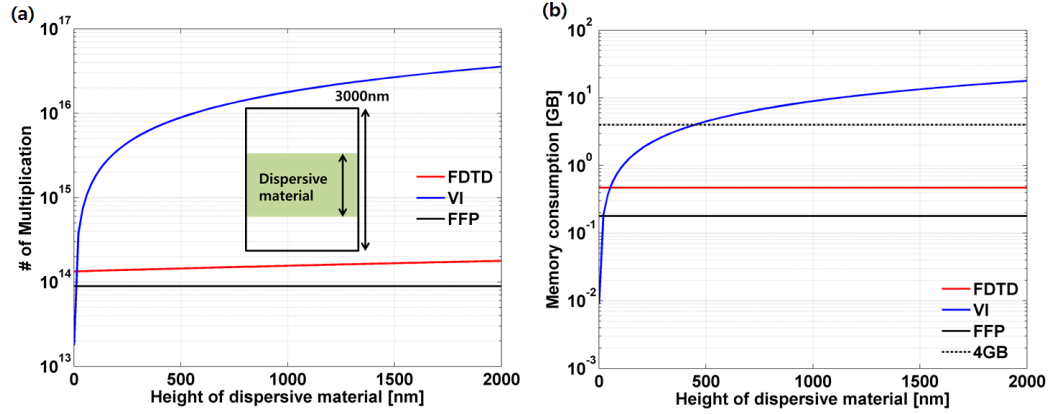
Fig. 2. Computational cost of the main FDTD algorithm, the volume integration (VI) method and the proposed flexible flux plane (FFP) method. Note that transmission and reflection spectra can be computed either by combining FDTD with VI or FDTD with FFP. The cost is calculated for $100 \times 100 \times 300$ cells with varying thickness (0—200 cells) of the dispersive material. A 10 nm grid spacing is assumed along all axes. (a) The number of multiplication operators used in each method versus dispersive material height. The inset figure represents the simulation geometry. (b) Memory consumption of each method versus dispersive material height.

demonstrated great potential to help quantify optical parasitic losses [14–16]. Specifically, finite difference time domain (FDTD) methods can employ the integral of the power loss over the volume of the photovoltaic materials to quantify the fraction of useful and parasitic optical absorption at any layer of the solar cells [17]. Unfortunately, this volume integration (VI) method increases the time complexity of the FDTD algorithm to a higher order. This makes optimization based on the FDTD method extremely slow and computationally expensive. [18–21]. Due to this critical limitation of the VI method, most previous simulations were conducted only within very thin layers (100—300 nm thick) [14, 16, 17] and limited wavelength ranges ($\lambda =$ 600—800 nm) [22]. A promising approach to sidestep this great computational expense would use flat flux planes [23] surrounding the volumes of interest, such as sets of flux planes forming a cube [24], or flux planes in the middle of a cell [15]. However, the geometries allowed by this method are still limited to boxlike shapes.

In this work, we propose a novel simulation technique that can quantify the absorption in complicated (or generalized) 3-D cell structures both within a reasonable amount of computational time and with a negligible amount of memory consumption. Figure 2 indicates the computational cost of the main FDTD algorithm (without absorption), the VI method and the proposed method. The number of multiplication operations is nearly proportional to the computational time of the algorithm. As shown in Fig. 2(a), the VI method significantly delays the original FDTD method when the enclosed photovoltaic material is a few hundred nanometers thick. Also, the memory consumption of the VI method exceeds 4 GB, a common limit for RAM per computational core, when the thickness of the material is larger than 500 nm. This calculation is based on the grid size of 10 nm; a smaller grid size will increase the computational burden of the volume integration method. However, in the proposed method, both the speed of algorithm and the memory consumption are well below the original FDTD algorithm, so it does not significantly delay the main FDTD computation.

In this work, the proposed simulation technique will be discussed in detail, and then verified through a detailed comparison to experimental thin-film c-Si light trapping structures from

(a)
Surface Integration of Flux (SI)
$O(N_s^2 \times N_w)$

(b)
Volume Integration of Flux (VI)
$O(N_s^3 \times N_w)$

(c)
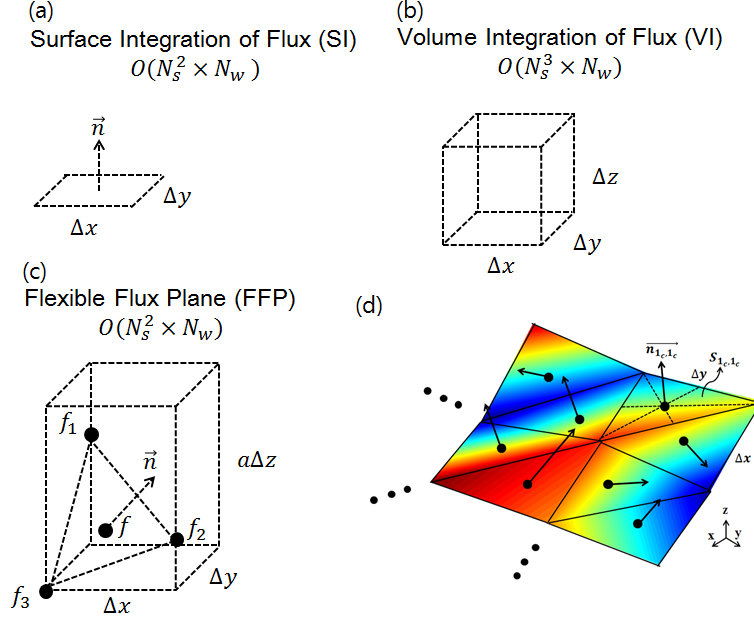Flexible Flux Plane (FFP)
$O(N_s^2 \times N_w)$

(d)

Fig. 3. Schematic illustration of methods of measuring flux density in the simulations: (a) A traditional approach to calculate transmitted and reflected power in FDTD simulations. The computation time goes as $\mathcal{O}(N_s^2 \times N_\omega)$, where N_s as the number of grid points in each spatial direction, as well as the total number of distinct frequencies; (b) The volume integration method, which separates different source of optical losses in the simulation – this method is considerably slower, and goes as $\mathcal{O}(N_s^3 \times N_\omega)$; (c) Flexible flux planes, for rapid, frequency-sensitive integration of parasitic losses, represent a generalization of the flux plane in (a). In each Yee cube, an arbitrary surface is closely approximated (if not exactly represented) by a pair of triangles with the same center and normal vector. Local field values are interpolated from the nearest six fields fixed on the Yee lattice; (d) The expanded schematic structure of the flexible flux planes in the x-y plane – an arbitrary surface can be approximated by this method.

Fig. 1. Next, an improved light trapping scheme for 2 μm c-Si cells with lower parasitic losses is proposed, which combines a recently reported correlated random front surface [25] with a plasmonic back reflector (BR). Finally, the optimized result is compared with both the ideal Lambertian limit and a totally random structure with limited roughness feature heights.

2. Method

Since the FDTD method has been considered a promising tool for optical simulations, a great deal of work has been presented on improving the accuracy of this method [26–32]. The FDTD method generally represents curved material boundaries as stepped edges, resulting in discretization errors [27, 28]. One study used a contour FDTD method, which utilizes subpixel modeling to reduce this error. In this work, arbitrary surfaces of both metal and dielectric materials are considered. Then, we use a general tri-linear interpolation to reduce this discretization error.

2.1. Flexible flux planes

The surface integration of the Poynting vector (SI) over a flat plane successfully calculates the total absorption of solar cells within a moderate computational time and memory (compared to the propagation of Maxwell's equation) by this equation for the transmitted power [23]:

$$P_t = \vec{n} \cdot \sum_\omega \sum_i \sum_j \text{Re}[E_{\omega,i,j}^*(\vec{r}) \times H_{\omega,i,j}(\vec{r})], \tag{1}$$

where $\vec{r}$ is the location in 3-D space on the flat flux plane, $\vec{n}$ is a normal vector from the flat flux plane, $E_{\omega,i,j}(\vec{r})$ is Fourier-transformed electric field at the position of i, j and frequency ω, and $H_{\omega,i,j}(\vec{r})$ is Fourier-transformed magnetic field at the position of i, j and frequency ω. In FDTD simulations for solar cells, this computation is performed over relevant wavelengths, which range from 300 nm to the bandgap of PV material [1]. We can define N_s as the number of grid points in each spatial direction and N_ω as the total number of distinct frequencies. In this case, the flat flux plane method has $\mathcal{O}(N_s^2 \times N_\omega)$ time complexity, which is of the same order as the original FDTD calculations. Of course, FDTD is still $\mathcal{O}(M)$ with respect to the total number of voxels M in 3D, but $M = N_s^3$ as defined here. However, typically the flux plane calculation is generally slightly faster than the FDTD propagation, in the common case where only a subset of all possible frequencies below the Nyquist limit are of interest.

For problems concerning irregular shapes that cannot be solved with the flat flux plane approach, let us now consider the more general energy loss calculation by the VI method:

$$P_{loss} = \sum_\omega \frac{1}{2} \varepsilon''(\omega) \varepsilon_0 \sum_i \sum_j \sum_k |E_{\omega,i,j,k}(\vec{r})|^2, \tag{2}$$

where ε'' is an imaginary part of PV material. This method is performed over both the active PV volume and frequency, corresponding to $100 \times 100 \times 200 \times 200$ ($N_s^3 \times N_\omega$) for 2 μm thick silicon material. As shown in Fig. 2(a), the higher order $\mathcal{O}(N_s^3 \times N_\omega)$ of computational time of VI method now significantly delays the original FDTD algorithm $\mathcal{O}(N_s^3)$. Also, the memory storage is increased from a three dimensional data structure (x, y, ω) to a four dimensional data structure (x, y, z, ω), making volume integration of losses within FDTD an extremely expensive approach.

To overcome the computational burden of the VI method while preserving its flexibility, we now introduce a flexible flux plane (FFP) method, whose computational time is just $\mathcal{O}(N_s^2 \times N_\omega)$ for arbitrary surfaces, with a speed similar to that of the flat flux planes, but with generality comparable to that of volume integration. As shown in Fig. 3(c), the FFP method assumes that there is a pre-defined material boundary, which is discretized into triangles within the Yee grid. Then, as shown in Fig. 3(d), it calculates the centroid points of the triangles, their normal vectors, and their cross-sectional areas. Note that these calculations are performed only once (before FDTD starts its time iteration), so they do not affect the computational time of the main FDTD loop. Using predefined information, FFP now tracks the net transmitted electromagnetic flux along a material boundary in time iteration of a FDTD simulation with a given calculation of the transmitted power:

$$P_t = \sum_\omega \sum_i \sum_j \vec{n}_{i_c,j_c} \cdot \text{Re}[E_{\omega,i_c,j_c}^*(\vec{r}) \times H_{\omega,i_c,j_c}(\vec{r}) \cdot S_{i_c,j_c}], \tag{3}$$

where $\vec{n}_{i_c,j_c}$ is a normal vector at the i_{th}, j_{th} sub-triangle of Yee's grid, $E_{\omega,i_c,j_c}(x)$ is the time Fourier-transformed incident field at the centroid point i_c, j_c and S_{i_c,j_c} is an area of the i_{th}, j_{th} sub-triangle. To guarantee second-order accuracy, FFP interpolates both fields to the centroid point before applying Eq. (3). As shown in Fig. 2(b), the FFP calculation does not significantly

burden the computational time, because it is only performed at the material boundary, which results in $\mathscr{O}(N_s^2 \times N_\omega)$ complexity. As explained in this work, the FFP approach is relatively straightforward to implement, so it is applicable to all FDTD tools (in principle).

2.2. *Parasitic absorption modeling*

Traditional approaches to enhancing light trapping in thin-film solar cells are illustrated in Fig. 1. In these approaches, incident rays are scattered at the front texturing surface into the active Si material, or toward the Ag BR while potentially exciting the surface propagating polariton (SPP) mode. A large fraction of the SPP and transmitted rays are eventually absorbed by the Ag BR, causing parasitic absorption. In this modeling section, J_{sc} and J_{par} are calculated by

$$ J_{sc} = \int_0^\infty d\lambda \left[\frac{e\lambda}{hc} \frac{dI}{d\lambda} A_{total}(\lambda) IQE(\lambda) \right], \text{ and} \tag{4} $$

$$ J_{par} = \int_0^\infty d\lambda \left[\frac{e\lambda}{hc} \frac{dI}{d\lambda} A_{par}(\lambda) IQE(\lambda) \right], \tag{5} $$

where J_{sc} is the useful short circuit current density, J_{par} is the parasitic current density, $\frac{dI}{d\lambda}$ indicates the solar spectrum given by AM1.5G, $A_{total}(\lambda)$ represents the total absorption calculated under short circuit conditions by $A_{total}(\lambda) = 1 - R(\lambda) - T(\lambda)$, $IQE(\lambda)$ represents internal quantum efficiency, $A_{par}(\lambda)$ represents the parasitic absorption calculated by $A_{par}(\lambda) = T_{FFP}(\lambda) - T(\lambda)$ and $T_{FFP}(\lambda)$ represents the net transmitted power along the flexible flux plane, and $R(\lambda)$ and $T(\lambda)$ represent the reflected power and the transmitted power, respectively, observed at the vertical ends of the simulation domain. Note that the charge collection losses are considered in section 3 for comparison with the experiment; later, in section 4, they are neglected to estimate upper limits of performance. IQEs were calculated by combining measurements of EQE and total reflection using a standard definition (IQE = EQE/(1-R)). In order to compare the experimental total absorption with simulated results, all absorption plots show total absorption ($A(\lambda) = 1 - R(\lambda) - T(\lambda)$), which includes parasitic absorption, while the parasitic absorption is still given by $T_{FFP}(\lambda) - T(\lambda)$.

In order to accurately model the behavior of the materials used in the experiments (such as c-Si and silver), a recently developed time-domain dispersion model, called quadratic complex rational function (QCRF), is used [25, 33]. Other experimental materials of interest (e.g., ZnO and ITO) were assumed to be non-dispersive and non-absorptive, since thin ITO and ZnO layers generally appear transparent in the visible wavelengths and their single path absorption of 70 nm ITO does not exceed 2.42% for near-infrared wavelengths below 1000 nm. The overall impact of realistic dispersion on the short-circuit current is relatively modest for sample cells, not exceeding 0.6 mA/cm^2 for the designs tested in the next section, and are not highly sensitive to the cell design. Thus, ITO dispersion is not included in our subsequent analysis. Sources are placed above the cell, perfectly matched layers are imposed at the vertical ends, and because the photovoltaic cells are very large in the transverse direction, periodic boundary conditions are applied in the transverse directions with 1 μm periodicity. The spectrum of incident waves considered ranges from 400 nm to 1100 nm (close to the band edge of silicon).

3. Result : modeling of experimental light trapping approaches

3.1. *Periodically textured texturing cell*

As illustrated in Fig. 1(a), periodically textured cells diffract incoming light into highly localized modes inside the active Si material. Commonly, periodic (grating like) cells are deposited
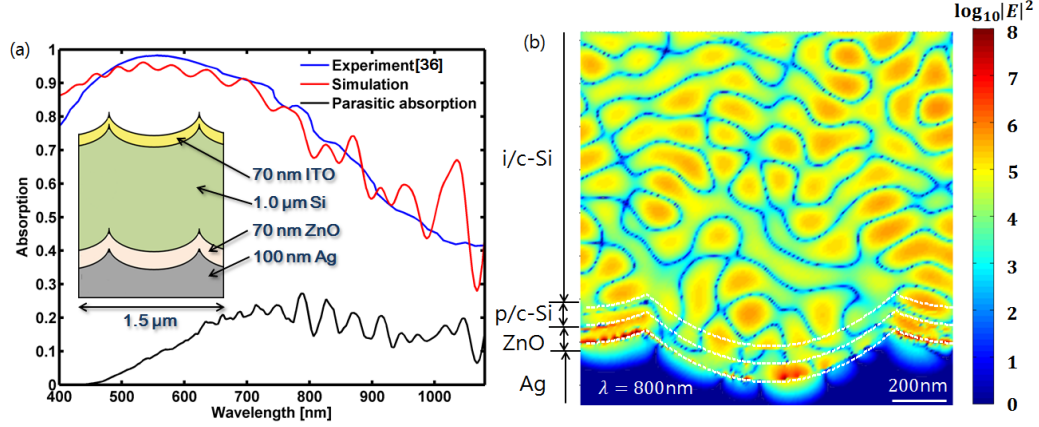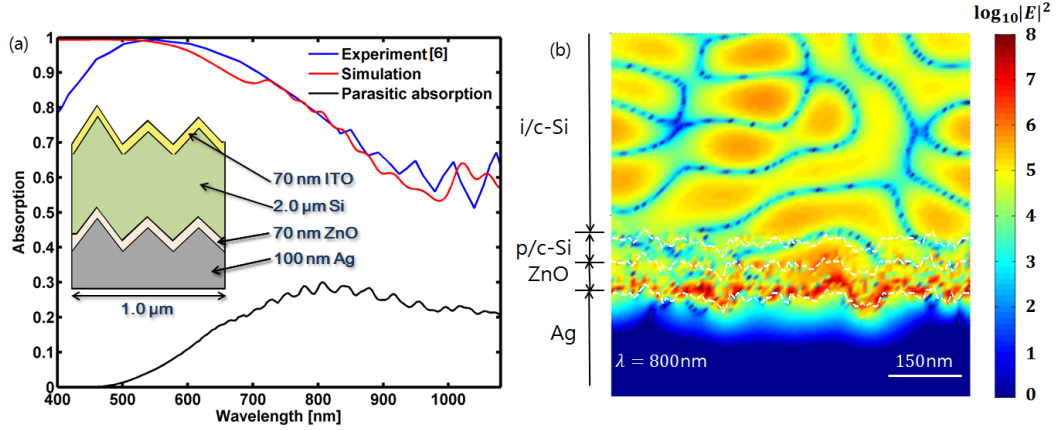
Fig. 4. Light trapping results for periodically textured conformal 1.0 μm-thick thin-film c-Si solar cells: (a) The experimental [36] and 3-D FDTD-simulated total absorption, which agree closely. Parasitic absorption is calculated by the proposed method; the total amount corresponds to 4.05 mA/cm^2. The inset figure shows the simulation geometry. The super-cell has 1.5 μm periodicity; (b) Electric field intensity near the bottom part of the cell at the yz plane at $\lambda = 800$ nm on a log scale. Field intensity is normalized by the incident field. A highly localized electric field is observed near the silver back reflector, over a hundred times stronger than the active region. The localized field could be either propagating along the surface, or stationary near the edge of the random back reflector.

conformally, thus the front and back surfaces have similar morphologies [7, 8, 34, 35]. The experimental periodic texturing cells typically have a simple pattern on the back surface, which may not excite strong SPP modes, but they still have a few edges on their BRs, which may introduce localized fields near these edges.

Modeling the 3-D experimental periodically textured solar cells in FDTD simulations is challenging, since true experimental cells have roughness and randomness that departs from ideal periodicity. Our modeled cells have a structure consisting of 1-μm-thick c-Si textured with a 1.5 μm period and a nearly parabolic shape shown in the inset of Fig. 4(a), which is very close to the experiment structure in [36]. In our model, the quantified useful J$_{sc}$ was 24.21 mA/cm^2 and J$_{par}$ was 4.05 mA/cm^2. This compares reasonably well to the reported J$_{sc}$ of 25 mA/cm^2 in [36], with an error of 3.6 % relative. As shown in Fig. 4(b), high field intensities are observed near the surface of the Ag BR in the form of a standing wave. Our calculations using the FFP method indicate that the strong overlap of these standing waves with Ag causes substantial parasitic losses.

To quantify the role of material thickness in the periodically textured design, and for ease of comparison with other experiments, we modeled the effect of increasing the average thickness of crystalline silicon from the experimental value of 1 μm to a value of 2 μm, which was also used in the random texturing and plasmonic cells. In this case, we found that the useful J$_{sc}$ increases from 24.21 mA/cm^2 to a value of 26.04 mA/cm^2.

The degree of light trapping observed may be sensitive to the maximum height of the surface features. We investigated this sensitivity by choosing a 2 μm-thick cell having a constant period of 2.5 μm, the best value observed in experiment [36]. We then varied the periodic texture height in a range from 0 to 625 nm, and found that the best height value was 500 nm, much like in the experiment. In this case, the useful J$_{sc}$ improved to 26.04 mA/cm^2, while J$_{par}$ dropped to 3.77 mA/cm^2. Since the 2-μm-thick periodic texturing cell has the same thickness with the

other cells which will be studied in the next sections, it could be directly compared to other cells.

3.2. Random texturing cell

Random texturing on the front and back surfaces provides another pathway toward enhancing light trapping. As shown in Fig. 1(b), the typical random texture is deposited conformally [6]. As mentioned earlier, the random surface at the front can enhance light trapping up to the Yablonovitch limit; however, the back side texturing may give rise to both light trapping enhancement and increased parasitic loss. Thus, in this section, we apply the FFP method to quantify the amount of parasitic loss occurring in randomly textured cells.

Fig. 5. Light trapping results for randomly textured conformal 2.0 μm thin-film c-Si solar cells: (a) The experimental [6] and 3-D FDTD-simulated total absorption, which agree closely. Parasitic absorption is calculated by the proposed method; the total amount corresponds to 5.16 mA/cm^2 in this case. The inset figure shows the simulation geometry. The supercell has 1 μm periodicity. The random texturing surface is generated by a correlated randomness algorithm [25], with maximum feature heights varying from 300 to 1000 nm; (b) Electric field intensity near the yz plane at $\lambda = 800$ nm on a log scale. Field intensity is normalized by incident field. A highly localized electric field was observed near the silver back reflector, over a hundred times stronger than the active region. The localized field could be either propagating along the surface, or stationary near the edge of the random back reflector.

We modeled a conformal random texturing cell with 2 μm thickness (sample D in [6]). Since random textures will have random variations over small spatial regions, resulting in random spectral features, we must generate an ensemble of many random surfaces and average the results to converge on the large-area limit for light trapping. After 50 identical trials, we calculate the average useful J_{sc} to be 22.77 mA/cm^2 in 2-μm-thick c-Si solar cells, while the average J_{par} to be 5.16 mA/cm^2, with a standard error below 1 mA/cm^2. This predicted useful J_{sc} matches well with the spectrally-integrated experimental EQE data for sample D in [6], which corresponds to a J_{sc} of 22 mA/cm^2 for a relative error of 3.5 %. We avoid directly using the measured J_{sc} from the I-V curve because the additional complications associated with masking, the choice of solar simulator spectrum, and the overall solar simulator power go beyond the scope of this study. The total ensemble-averaged absorption predicted by our model matches the experiment very closely, as shown in Fig. 5(a). The amount of parasitic absorption was very substantial in the presence of a highly textured Ag BR. As shown in Fig. 5(b), strong localized fields are observed near the Ag BR, which may introduce strong SPP modes. Based on these

observations, it appears that rough surfaces in the BR generally cause high parasitic losses. The mechanisms for rough surfaces enhancing losses may include SPP mode coupling and slow-light propagation near the metal surface; based on the large value of our ensemble-averaged random texture J_{par}, it may be hard to avoid both mechanisms simultaneously.

On a related note, Sivec et al. recently demonstrated a promising random texturing method using a ZnO pre-coating to independently control ZnO and Ag surface morphologies [37]. To explore the light trapping potential of a random texturing approach, we optimized the ZnO and Ag surfaces separately and then combined them with the front surface random texturing including the internal quantum efficiency from sample D in [6]. We found that the best random textured 2-μm-thick cell could achieve 27.41 mA/cm^2 J_{sc} with 3.11 mA/cm^2 parasitic loss. A general improvement in the amount of useful absorption is consistent with the experimental observations of improved maximum power in [37]. The optimized structure we calculated has relatively high texturing features on the front, moderate texturing features on the ZnO layer and small texturing features on the Ag layer. The important observation here is that although the metal back reflectors are slightly textured (feature heights of approximately 50 nm), the parasitic loss quantified in this type of cell was not negligible. This implies that in future studies of nano-structured BRs, it will be essential to determine the fraction of useful absorption and parasitic absorption to prove that the benefits of a new approach outweigh its disadvantages.

3.3. Plasmonic cell

The last type of experimental thin-film c-Si cell considered in this manuscript, shown in Fig. 1(c) is a plasmonic enhanced cell with a hemispherical rear Ag NP [11]. Recently, it has been demonstrated that this specific structure can greatly improve light trapping in thin silicon solar cells [10, 11, 38]. In this approach, light trapping can be achieved both by the front surface and the back NP, but it also has two sources of parasitic absorption; the Ag NP and the Ag BR. The parasitic losses of the plasmonic NPs are a particular problem for this type of light trapping approach [39, 40]. Thus, we quantify the total amount of parasitic losses in these plasmonic type cells by placing our proposed FFP right at the Si/ZnO boundary.

We have modeled the performance of a hemispherical Ag plasmonic NP using FFP. The modeled experimental structure, whose performance was described in Fig. 4(a) in [11], has a single 600 nm diameter NP in 1 μm periodicity and 200 nm thick ZnO layer encapsulating the NP. As shown in Fig. 6(a), and in contrast with other light-trapping techniques, the hemispherical NP embedded in ZnO does not create large parasitic losses. As shown in Fig. 6(b), the hemispherical NP does introduce a localized field around its surface, but it does not propagate along the surface of the NP as SPP modes – possibly because these NPs are physically separated from one another. Note that the absorption enhancement observed in excess of the experimental data in Fig. 6(a) is due to two differences between the simulation and experiment, in terms of periodicity and texturing. First, the simulation incorporates very small front surface texturing features not found in experiment that increase the short wavelength absorption (i.e., around 400 nm). Second only the simulated structure has a periodic arrangement of NPs in the ZnO layer, which strongly enhances absorption near the diffraction threshold (around 1100 nm). Nonetheless, 50 identical simulation trials of these cells yield J_{sc} =24.01 mA/cm^2, which is only a 0.01 % error from the reported J_{sc} with 2.04 mA/cm^2 of parasitic loss; this result demonstrates that these two errors effectively cancel. This in turn strongly indicates that the plasmonic rear NP does not introduce much parasitic loss, while successfully enhancing the absorption of the cell.

4. Result : Optimization toward the Lambertian limit

Further improvement of useful absorption for experimentally relevant solar cells may be achieved through optimization of three factors; the front scattering surface, the overall peri-
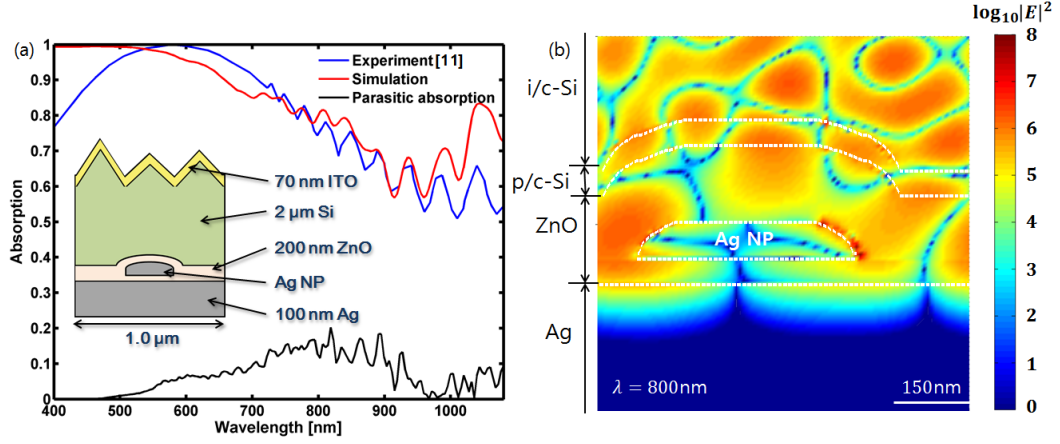
Fig. 6. Light trapping results for 2.0 μm thick c-Si solar cells using plasmon enhanced BRs (plasmonic particles of 600 nm diameter and 150 nm height); (a) The experimental [11] and 3-D FDTD-simulated total absorption, which agree well for most wavelengths. Total parasitic absorption is calculated to be 2.04 mA/cm^2, while the amount of useful absorption is 24.01 mA/cm^2. The inset figure shows the simulation geometry. The supercell has 1 μm periodicity; (b) Electric field profile at the yz plane at $\lambda = 800$ nm in log scale. Field intensity is normalized by the incident field. A highly localized electric field was observed near the edge of the Ag NP.

odicity, and the back reflector. As mentioned previously, new deposition techniques have made it possible to control the surface of each layer separately [37] and deposit NPs between the layers. This capability could be used to improve the front scattering surface further with correlated random texturing for thin-film micromorph tandem cells, which was demonstrated by the current authors to outperform a pure random texturing over a broad range of wavelengths [25]. This front surface design introduces short-range correlations to capture the smoothness of real structures, as well as periodicity to enhance diffraction into waveguided modes that are strongly absorbed [41, 42]. These results provide a concrete basis for detailed structural design and optimization. Note that in this section, we obtain a partial fraction of light absorption of silicon layer by FFP method, which is then multiplied by both an ideal IQE (without charge collection losses), and the AM1.5G solar spectrum to calculate $J_{sc,ideal}$ and $J_{par,ideal}$:

$$J_{sc,ideal} = \int_{300nm}^{1100nm} d\lambda \left[\frac{e\lambda}{hc} \frac{dI}{d\lambda} A_{Si}(\lambda) \right], \text{ and} \qquad (6)$$

$$J_{par,ideal} = \int_{300nm}^{1100nm} d\lambda \left[\frac{e\lambda}{hc} \frac{dI}{d\lambda} A_{par}(\lambda) \right] \qquad (7)$$

where $J_{sc,ideal}$ is the short circuit current density calculated under an ideal IQE, and $J_{par,ideal}$ is the parasitic current density calculated under an ideal IQE, $A_{Si}(\lambda)$ is the partial fraction of light absorption of silicon layer by the FFP method. This assumption of an ideal quantum efficiency is utilized because an experimentally measured IQE may not accurately reflect minimal parasitic absorption in our cell designs, and to clearly demonstrate the theoretical limits of our optical design.

In our first investigation, we combine the experimental structure from Section 3.3 with a correlated random surface in the front, and compare it with a control, consisting of an identical front random surface and a flat BR. Starting with a 2-μm-thick c-Si cell, two 1 μm-periodic
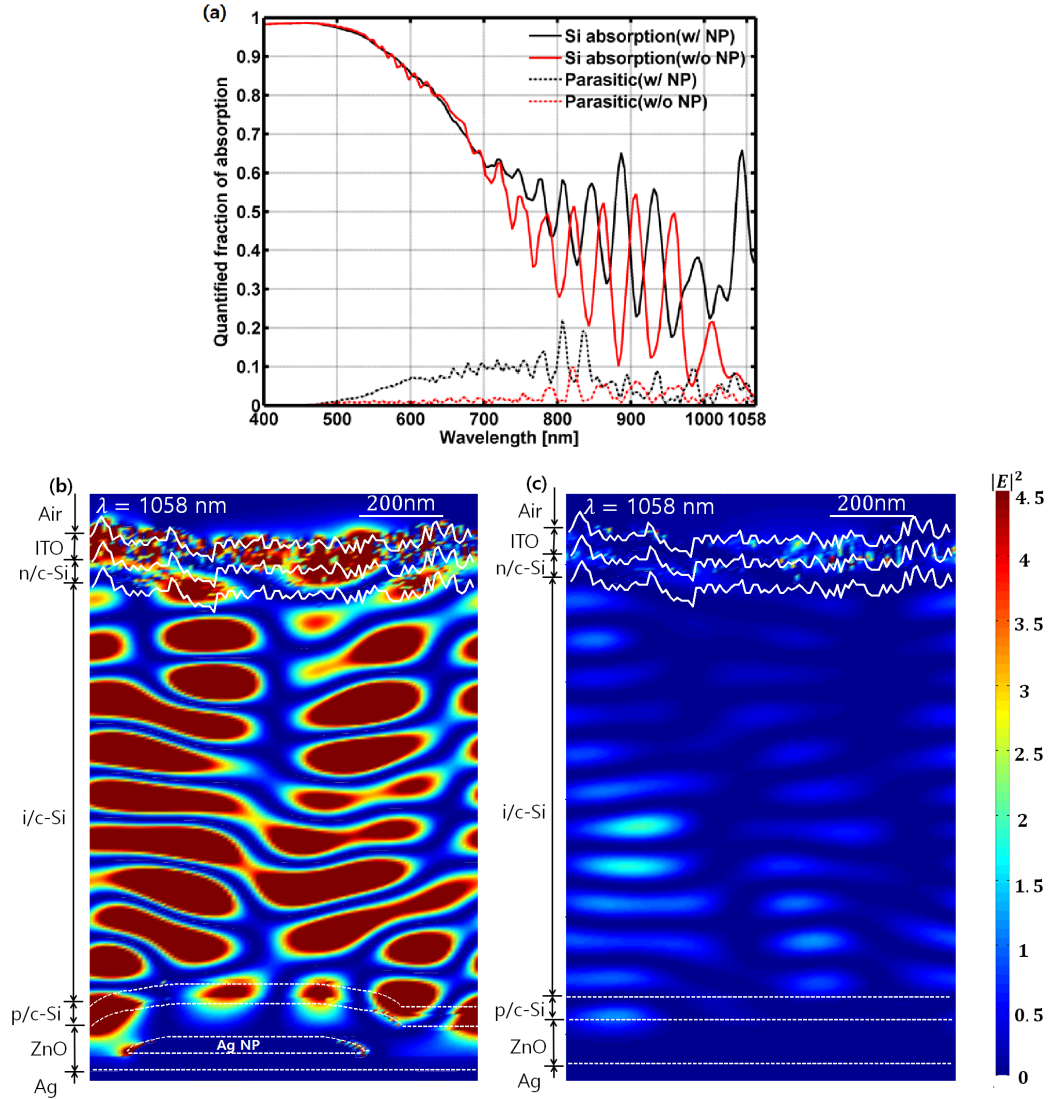
Fig. 7. (a) Useful absorption $(1 - R - T_{FFP})$ and parasitic absorption $(T_{FFP} - T)$ spectra for a correlated random front surface combined with a plasmonic rear NP (black), and those spectra for an identical front surface combined with a flat BR (red). (b) Electric field profile of the cell with the NP at $\lambda = 1058$ nm (c) Electric field profile of the cell without the NP at $\lambda = 1058$ nm. Both field profiles have the same scale bar.
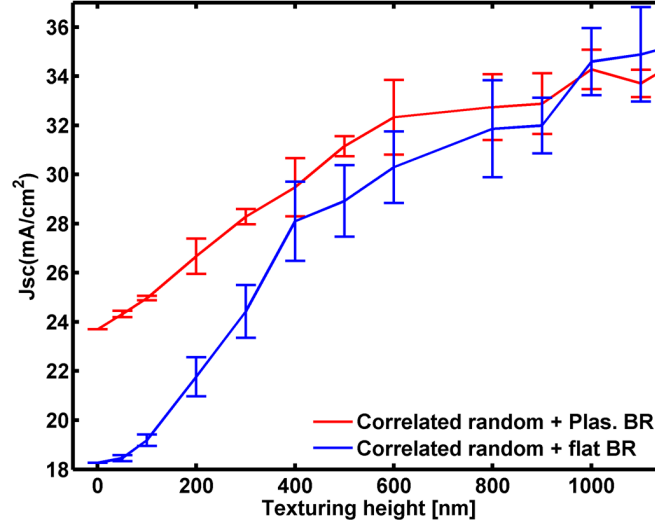
Fig. 8. Optimized short circuit current as a function of texture height in two structures: first, a correlated random front texturing combined with a plasmon-enhanced BR (red) and second, an identical random front combined with the flat BR (blue). Standard errors are calculated for both curves using 5 identical trials. In the small texturing cells, the plasmonic NP gives rise to good light trapping with minimal parasitic loss. Once the correlated random front texturing achieves strong light trapping, the contribution of plasmonic NP gradually decreases, and finally saturates for highly textured cells.

features are included: a 300 nm-high textured front surface created by the correlated random algorithm [25] and a rear NP with a 600 nm diameter. In Fig. 7(a), at longer wavelengths (over 700 to 1100 nm), nearly 20 % relative absorption enhancement is observed on average from combining the correlated random and rear NP features while, at shorter wavelengths, no meaningful enhancement is observed. Note that the solid red and black curves only include useful absorption of light in the silicon. In Figs. 7(b) and (c), the electric field profiles are shown for the nanoparticle and control (flat BR) cases, respectively, at a wavelength of 1058 nm. Even though they have the same front texturing, strong light trapping modes are observed only in the first case (with NP). Compared to the flat BR case, the rear NP does not introduce additional parasitic modes, but still strongly enhances absorption in this wavelength region.

In our second study, we consider the effects of varying the various diameters of NPs (100—800 nm) placed within the rear ZnO layer. If we combine this with a correlated random surface and a periodicity of 1 micron, we find that a 600 nm diameter yields the best value of $J_{sc,ideal}$. Next, we optimize the correlated random front surface with respect to the feature height, when combining it with the best Ag NP geometry. The results are compared with cell structures having identical front texturing but a flat BR. In both cases, multiple simulations are performed for each texturing height, and the results are averaged to reduce the random fluctuation of $J_{sc,ideal}$. As shown in Fig. 8, the rear NP improves $J_{sc,ideal}$ by nearly 6 mA/cm^2 in the flat front case. Note that the parasitic loss is already subtracted off our result, and does not exceed 4 mA/cm^2 due to its flat BR. The standard errors in each case are calculated as the quotient of the standard deviation and the square root of the number of identical trials n for each parameter value (here, $n = 5$) [43]. This result is then graphed as error bars for each curve and parameter value, as can be seen in Fig. 8. As the silicon thickness and thus absorption increases, the importance of the rear NP for light trapping decreases. Eventually, both $J_{sc,ideal}$ curves plateau for texturing
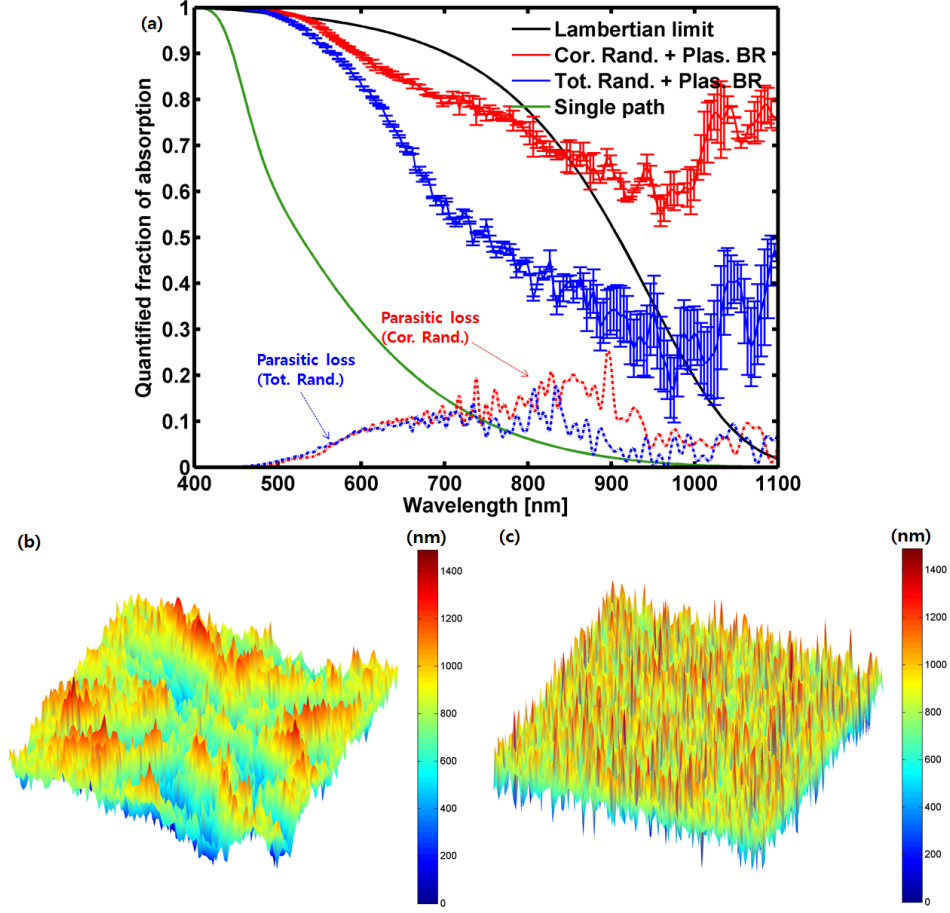
Fig. 9. (a) Useful and parasitic absorption spectra calculated for 2 μm thick c-Si solar cells with ideal light-trapping. The red solid curve means the fraction of useful absorption in the correlated random front surface with a plasmon enhanced BR, and the blue solid curve means the fraction of useful absorption in the pure random front texturing with a plasmon enhanced BR. Standard errors are calculated for both curves using 5 identical trials. Absorption of the optimized cells exceed the Lambertian limit at higher wavelengths and out-performs the purely random cells as well. Note that the parasitic absorption is pre-subtracted and plotted. $J_{par,ideal}$ at the optimized structure is 3.74 mA/cm^2 and the reflected loss is 4.97 mA/cm^2, while $J_{sc,ideal}$ is 36.60 mA/cm^2, which exceeds the Lambertian limit; (b) Front surface morphology of the optimized correlated random structure; (c) Front surface morphology of the pure random structure.

heights greater than 1200 nm (not shown). This implies that in the presence of an ideal front scatterer, an additional back scatterer is unnecessary to enhance light trapping. However, since most experimental light trapping cells still suffer incomplete light absorption at wavelengths ranging from 700 to 1100 nm, which is driven by the limited availability of texturing heights and periods, it is still worth considering the plasmonic type BR with experimentally available texturing methods.

Finally, the performance of the optimal cell combining correlated random front texturing with a rear NP structure is presented in Fig. 9(a) as a solid red curve, and compared to competing

light trapping strategies. This result is unique, because many previous researchers in light trapping have focused on total absorption, but do not subtract parasitic losses. In contrast, our result only includes useful absorption. The quantified $J_{sc,ideal}$ of the optimum cell is 36.60 mA/cm^2 with 3.74 mA/cm^2 parasitic loss and 4.97 mA/cm^2 reflected loss; this compares favorably with the Lambertian limit of an ideal random light-trapping structure in a 2 μm thick c-Si cell of around 35 mA/cm^2 [12]. Now let us consider the physical structure of this optimal absorber after accounting for parasitic losses. It is smooth over short distances, yet offers the large features required to support strong light-trapping modes, as shown in Fig. 9(b). By comparison, the purely random structure, shown in Fig. 9(c), has very narrow features densely distributed on the surface. Overall, our optimization results in this section have demonstrated that a front random scatterer can enhance broad-band absorption while the additional periodicity and a rear NP can enhance absorption at targeted wavelengths, particularly near the band edge. These principles are general, and can be applied to a broad range of PV materials, particularly indirect bandgap materials, with appropriate adjustments to the NP geometry.

5. Conclusion

In conclusion, a new simulation technique, called flexible flux plane (FFP) finite-difference time-domain (FDTD) is introduced in this manuscript. FFP FDTD allows one to accurately calculate parasitic losses in thin-film c-Si solar cells, while reducing time and memory consumption by two orders of magnitude compared to volume integration-based approaches. Applying this technique to experiment, three particular types of well-characterized light-trapping photovoltaic cells have been accurately modeled. First, conformally deposited periodic cells were shown to have moderate parasitic losses (4.05 mA/cm^2) with good total absorption. Second, conformally deposited random cells were demonstrated to have the highest parasitic losses (5.16 mA/cm^2) due to their rough metal back surfaces. Third, the flat Ag BR with a rear NP structure was shown to have the lowest parasitic losses (2.04 mA/cm^2), with a strong absorption peak around higher wavelengths. This last structure was then combined with a correlated random front texture and optimized for the case of ideal charge collection to achieve the highest possible J_{sc}. It was found that the 600 nm diameter NP strongly enhances light absorption at wavelengths ranging from 700 nm to 1100 nm, while a correlated random surface has much broader absorption enhancement. In our optimized result, 36.60 mA/cm^2 $J_{sc,ideal}$ is achieved only with 3.74 mA/cm^2 of parasitic loss. This result is slightly above the Lambertian limit of 2 μm thick silicon cells, even after including parasitic losses. However, this structure requires nanoscale structural control and high-performance thin-film electronic materials to fully realize this prediction.